Title

Automated assessment of the remineralization of artificial enamel lesions with polarization-sensitive optical coherence tomography

Journal

Biomedical Optics Express, 5(9)

ISSN

2156-7085

Authors

Lee, Robert C
Kang, Hobin
Darling, Cynthia L
et al.

Publication Date

2014-09-01

DOI

10.1364/boe.5.002950

Peer reviewed

Biomedical Optics EXPRESS

Automated assessment of the remineralization of artificial enamel lesions with polarization-sensitive optical coherence tomography

Robert C. Lee, Hobin Kang, Cynthia L. Darling, and Daniel Fried*

Department of Preventive and Restorative Dental Sciences, University of California, San Francisco, 707 Parnassus Ave, San Francisco, CA 94143 USA

**daniel.fried@ucsf.edu*

Abstract: Accurate measurement of the highly mineralized transparent surface layer that forms on caries lesions is important for diagnosis of the lesion activity because chemical intervention can slow or reverse the caries process via remineralization. Previous *in-vitro* and *in-vivo* studies have demonstrated that polarization-sensitive optical coherence tomography (PS-OCT) can nondestructively image the subsurface lesion structure and the highly mineralized transparent surface zone of caries lesions. The purpose of this study was to develop an approach to automatically process 3-dimensional PS-OCT images and to accurately assess the remineralization process in simulated enamel lesions. Artificial enamel lesions were prepared on twenty bovine enamel blocks using two models to produce varying degree of demineralization and remineralization. The thickness of the transparent surface layer and the integrated reflectivity of the subsurface lesion were measured using PS-OCT. The automated transparent surface layer detection algorithm was able to successfully detect the transparent surface layers with high sensitivity (= 0.92) and high specificity (= 0.97). The estimated thickness of the transparent surface layer showed a strong correlation with polarized light microscopy (PLM) measurements of all regions (R^2 = 0.90). The integrated reflectivity, ΔR, and the integrated mineral loss, ΔZ, showed a moderate correlation (R^2 = 0.32). This study demonstrates that PS-OCT can automatically measure the changes in artificial enamel lesion structure and severity upon exposure to remineralization solutions.

OCIS codes: (170.4500) Optical coherence tomography; (170.1850) Dentistry; (170.0110) Imaging systems.

References and links

1. NIH, "Diagnosis and Management of Dental Caries throughout Life," pp. 1–24, NIH Consens. Statement (2001).
2. O. Fejerskov and E. Kidd, eds., Dental Caries: The Disease and its Clinical Management, Blackwell, Oxford (2003).
3. J. D. B. Featherstone, "Clinical Implications:New Strategies for Caries Prevention," Indiana University Early Detection of Dental Caries, pp. 287–296 (1996).
4. J. D. Featherstone, "The science and practice of caries prevention," J. Am. Dent. Assoc. **131**(7), 887–899 (2000).
5. J. M. ten Cate and J. D. B. Featherstone, "Mechanistic aspects of the interactions between fluoride and dental enamel," Crit. Rev. Oral Biol. Med. **2**(3), 283–296 (1991).
6. J. D. B. Featherstone, R. Glena, M. Shariati, and C. P. Shields, "Dependence of *in vitro* demineralization of apatite and remineralization of dental enamel on fluoride concentration," J. Dent. Res. **69**(Spec No), 620–625, discussion 634–636 (1990).
7. J. M. Cate and J. Arends, "Remineralization of artificial enamel lesions in vitro," Caries Res. **11**(5), 277–286 (1977).
8. E. A. Kidd, "The histopathology of enamel caries in young and old permanent teeth," Br. Dent. J. **155**(6), 196–198 (1983).

#213681 - $15.00 USD Received 9 Jun 2014; revised 25 Jul 2014; accepted 28 Jul 2014; published 1 Aug 2014

9. K. R. Ekstrand, D. T. Zero, S. Martignon, and N. B. Pitts, "Lesion activity assessment," Monogr. Oral Sci. **21**, 63–90 (2009).
10. H. Kang, C. L. Darling, and D. Fried, "Nondestructive monitoring of the repair of enamel artificial lesions by an acidic remineralization model using polarization-sensitive optical coherence tomography," Dent. Mater. **28**(5), 488–494 (2012).
11. R. S. Jones, C. L. Darling, J. D. Featherstone, and D. Fried, "Remineralization of in vitro dental caries assessed with polarization-sensitive optical coherence tomography," J. Biomed. Opt. **11**(1), 014016 (2006).
12. S. K. Manesh, C. L. Darling, and D. Fried, "Polarization-sensitive optical coherence tomography for the nondestructive assessment of the remineralization of dentin," J. Biomed. Opt. **14**(4), 044002 (2009).
13. A. Baumgartner, C. K. Hitzenberger, S. Dicht, H. Sattmann, A. Moritz, W. Sperr, and A. F. Fercher, "Optical coherence tomography for dental structures," SPIE Proceeding Vol. 3248, pp. 130–136 (1998).
14. A. Baumgartner, S. Dichtl, C. K. Hitzenberger, H. Sattmann, B. Robl, A. Moritz, A. F. Fercher, and W. Sperr, "Polarization-sensitive optical coherence tomography of dental structures," Caries Res. **34**(1), 59–69 (2000).
15. C. L. Darling, G. D. Huynh, and D. Fried, "Light scattering properties of natural and artificially demineralized dental enamel at 1310 nm," J. Biomed. Opt. **11**(3), 034023 (2006).
16. R. S. Jones and D. Fried, "The Effect of High Index Liquids on PS-OCT Imaging of Dental Caries," SPIE Proceeding Vol. 5687, pp. 34–41 (2005).
17. K. H. Nam, B. Jeong, I. O. Jung, H. Ha, K. H. Kim, and S. J. Lee, "Measurement of anisotropic reflection of flowing blood using optical coherence tomography," J. Biomed. Opt. **16**(12), 120502 (2011).
18. S. L. Chong, C. L. Darling, and D. Fried, "Nondestructive measurement of the inhibition of demineralization on smooth surfaces using polarization-sensitive optical coherence tomography," Lasers Surg. Med. **39**(5), 422–427 (2007).
19. D. Fried, J. Xie, S. Shafi, J. D. B. Featherstone, T. Breunig, and C. Q. Lee, "Early detection of dental caries and lesion progression with polarization sensitive optical coherence tomography," J. Biomed. Opt. **7**(4), 618–627 (2002).
20. R. S. Jones, C. L. Darling, J. D. Featherstone, and D. Fried, "Imaging artificial caries on the occlusal surfaces with polarization-sensitive optical coherence tomography," Caries Res. **40**(2), 81–89 (2006).
21. P. Ngaotheppitak, C. L. Darling, and D. Fried, "Polarization Optical Coherence Tomography for the Measuring the Severity of Caries Lesions," Lasers Surg. Med. **37**(1), 78–88 (2005).
22. C. Lee, C. L. Darling, and D. Fried, "Polarization-sensitive optical coherence tomographic imaging of artificial demineralization on exposed surfaces of tooth roots," Dent. Mater. **25**(6), 721–728 (2009).
23. R. S. Jones, C. L. Darling, J. D. B. Featherstone and D. Fried, "Remineralization of in vitro dental caries assessed with polarization sensitive optical coherence tomography," J. Biomed. Opt. **11**(1), 014016 (2006).
24. J. Arends, J. L. Ruben, and D. Inaba, "Major topics in quantitative microradiography of enamel and dentin: R parameter, mineral distribution visualization, and hyper-remineralization," Adv. Dent. Res. **11**(4), 403–414 (1997).
25. M. J. Everett, B. W. Colston, U. S. Sathyam, L. B. D. Silva, D. Fried, and J. D. B. Featherstone, "Non-invasive diagnosis of early caries with polarization sensitive optical coherence tomography (PS-OCT)," SPIE Proceeding Vol. 3593, pp. 177–183 (1999).
26. R. C. Lee, C. L. Darling, and D. Fried, "Automated detection of remineralization in simulated enamel lesions with PS-OCT," SPIE Proceeding Vol. 8929E, pp. 1–8 (2014).
27. L. M. Silverstone, J. S. Wefel, B. F. Zimmerman, B. H. Clarkson, and M. J. Featherstone, "Remineralization of natural and artificial lesions in human dental enamel in vitro. Effect of calcium concentration of the calcifying fluid," Caries Res. **15**(2), 138–157 (1981).
28. H. Yamazaki and H. C. Margolis, "Enhanced enamel remineralization under acidic conditions in vitro," J. Dent. Res. **87**(6), 569–574 (2008).
29. J. Bush, P. Davis, and M. A. Marcus, "All-Fiber Optic Coherence Domain Interferometric Techniques," SPIE Proceeding Vol. 4204, pp. 71–80 (2000).
30. H. Kang, J. J. Jiao, C. Lee, M. H. Le, C. L. Darling, and D. L. Fried, "Nondestructive Assessment of Early Tooth Demineralization Using Cross-Polarization Optical Coherence Tomography," IEEE J. Sel. Top. Quantum Electron. **16**(4), 870–876 (2010).
31. Y. K. Lee and W. T. Rhodes, "Nonlinear image processing by a rotating kernel transformation," Opt. Lett. **15**(23), 1383–1385 (1990).
32. K. H. Chan, A. C. Chan, W. A. Fried, J. C. Simon, C. L. Darling, and D. Fried, "Use of 2D images of depth and integrated reflectivity to represent the severity of demineralization in cross-polarization optical coherence tomography," J. Biophotonics. In press.
33. C. L. Darling, J. D. B. Featherstone, C. Q. Le, and D. Fried, "An automated digital microradiography system for assessing tooth demineralization," SPIE Proceeding Vol. 7162, pp. 1–7 (2009).
34. Y. Liu, S. Mai, N. Li, C. K. Yiu, J. Mao, D. H. Pashley, and F. R. Tay, "Differences between top-down and bottom-up approaches in mineralizing thick, partially demineralized collagen scaffolds," Acta Biomater. **7**(4), 1742–1751 (2011).
35. D. J. White, "The application of in vitro models to research on demineralization and remineralization of the teeth," Adv. Dent. Res. **9**(3), 175–193 (1995).
36. A. Thylstrup, C. Bruun, and L. Holmen, "In vivo caries models--mechanisms for caries initiation and arrestment," Adv. Dent. Res. **8**(2), 144–157 (1994).

#213681 - $15.00 USD Received 9 Jun 2014; revised 25 Jul 2014; accepted 28 Jul 2014; published 1 Aug 2014

37. A. Fercher, C. Hitzenberger, M. Sticker, R. Zawadzki, B. Karamata, and T. Lasser, "Numerical dispersion compensation for Partial Coherence Interferometry and Optical Coherence Tomography," Opt. Express **9**(12), 610–615 (2001).

1. Introduction

The caries process is potentially preventable and curable [1]. It is widely accepted that fluoride reduces the incidence of dental caries and slows or reverses the progression of existing lesions [2]. In addition to the fluoride therapy, other preventive measures such as anti-bacterial therapy, dietary changes or low intensity laser irradiation can be used as non-surgical means to arrest or reverse caries activity [1, 3]. Clinicians must be able to accurately diagnose lesion activity to establish the need for preventive treatment. Therefore, one cannot overstate the importance of accurate diagnosis of the caries activity in its early stage of development at which point non-invasive preventive measures can be taken to halt further decay.

Early caries lesions in enamel have a chalky white appearance with an intact surface layer [2]. The intact surface is of paramount importance because therapeutic intervention can arrest or reverse the process by remineralization [4]. Calcium and phosphate ions are lost from the tooth enamel during the demineralization process and the surface layer may erode with more severe acid challenge or mechanical abrasion and form a cavity [5]. During remineralization, there is growth of existing partially demineralized crystals as well as growth of new crystals within the lesion body due to the increased influx of calcium and phosphate ions [6]. The remnant crystal structure acts as a nucleation center for crystal growth. Fluoride plays a key role in the process of remineralization by enhancing the crystal growth and inhibiting future demineralization at the crystal surface. Remineralization therapy via fluoride produces fluorapatite crystals that are much more resistant to acid challenge than the original hydroxyapatite of enamel and dentin. With a thick enough fluorapatite layer, diffusion of calcium and phosphate ions at the lesion body, can be dramatically reduced [5, 7, 8]. This leads to the arrest of lesion progression and no further intervention is necessary.

The surface layer of a lesion is important for diagnosis of the current "state of the lesion", i.e., whether or not the caries lesion is active and expanding or whether the lesion has been arrested and is undergoing remineralization. Current methods for lesion assessment are composed of a combination of visual and tactile exams, which are prone to subjective bias, interference from staining, limitation to exposed surfaces and potential permanent damage to dental tissue from sharp instruments [1, 9]. In addition, the remineralized caries lesion still retains the white coloration due to the subsurface demineralization, which may lead to an inconclusive diagnosis of caries activity [9]. The gold standards for lesion assessment such as transverse microradiography (TMR) and polarized light microscopy (PLM) require destruction of the tooth, making both methods unsuitable for use *in-vivo*. New technologies are needed to determine whether caries lesions have been partially remineralized and have become arrested. Previous studies have demonstrated that PS-OCT is uniquely capable of this task since it provides a measurement of the reflectivity from each layer of the lesion and is able to show the formation of a zone of increased mineral density and reduced light scattering due to remineralization [10–12].

Polarization sensitivity is particularly valuable for resolving the structure of early caries lesions. PS-OCT images are typically processed in the form of phase and intensity images, and such images best show variations in the birefringence of the tissues [13, 14]. Caries lesions strongly scatter incident polarized light and the image in the orthogonal polarization axis to that of the incident polarization can provide improved lesion contrast. There are two mechanisms in which the intensity can arise in the cross-polarization axis. The native birefringence of the tooth enamel can rotate the phase angle of the incident light beam between the two cross-polarization axes as the light propagates through the enamel without changing the degree of polarization. The other mechanism is the scattering of incident light in

#213681 - $15.00 USD Received 9 Jun 2014; revised 25 Jul 2014; accepted 28 Jul 2014; published 1 Aug 2014

which the degree of polarization is reduced. It is this mechanism that is exploited to measure the severity of demineralization. Strong scattering of the incident linearly polarized light scrambles the polarization and leads to equal distribution of the intensity in both orthogonal polarization axes. Demineralization of the enamel due to dental decay causes an increase in the scattering coefficient by a 1-2 orders of magnitude [15]. This in turn causes a large rise in reflectivity in the cross-polarization axis. This approach also has the advantage of reducing the intensity of the strong surface reflection from the tooth allowing measurement of the lesion surface zone. A conventional OCT system is susceptible to strong Fresnel surface reflectance that can mask or resemble increased reflectivity from the lesion itself. Varying the angle of incidence and topical application of high index agents may be employed to mitigate the effect of the strong surface reflection in conventional OCT systems [16, 17]. The reflectivity in the cross-polarization OCT (CP-OCT) images can be directly integrated to quantify the lesion severity, regardless of the tooth topography. By using this approach the difficult task of deconvolving the strong surface reflection from the lesion surface from reflectivity from within the lesion can be circumvented. We have demonstrated in several studies that the lesion severity can be represented by the integrated reflectivity with depth in the CP-OCT image [12, 18–23]. The integrated reflectivity, ΔR, obtained from CP-OCT is a measurement analogous to the integrated mineral loss, ΔZ, obtained from TMR [24]. In contrast to most PS-OCT studies, which combine the images in both channels to generate images of phase and intensity, we utilize only the intensity in the cross polarization image to calculate ΔR [14, 25].

In our approach presented in ref [26], both polarization axes are required to determine the thickness of the surface zone. An accurate assessment of caries activity and severity is paramount for the clinical diagnosis of caries. Therefore, quantitative measurements of the transparent surface layer thickness and ΔR with PS-OCT are extremely valuable. In previous PS-OCT studies, we developed approaches to automatically quantify the severity of caries lesions and the depth of demineralized enamel for the rapid image processing of large 3D data sets [10]. In this study, we introduce and evaluate an approach to automatically process the OCT images to accurately detect and measure the thickness of the transparent surface layer in simulated enamel lesions that have undergone remineralization.

2. Methods

2.1 Sample preparation

Enamel blocks (n = 20), approximately 8–12 mm in length with a width of 2 mm and a thickness of 3 mm were prepared from extracted bovine incisors acquired from a slaughterhouse. Each enamel and bovine sample was partitioned into five regions or windows (1 sound and 4 lesion regions) by etching small incisions 1.8 mm apart across each of the enamel blocks using a laser. Incisions were etched using a transverse excited atmospheric pressure (TEA) CO_2 laser, an Impact 2500, GSI Lumonics (Rugby, UK), operating at 9.3 μm with a pulse duration of 15 μs, a pulse repetition rate of 200 Hz and a fluence of 20 J/cm^2. A thin layer of acid-resistant varnish in the form of nail polish, Revlon (New York, NY) was applied to protect the sound control area on each end of the block before exposure to the demineralization solution.

Artificial enamel lesions were prepared using two different methods in order to produce varying degree of demineralization and remineralization. The neutral pH remineralization model utilizes an undersaturated calcifying solution that has been shown to remineralize enamel more completely than a supersaturated calcifying solution [27]. The undersaturated solution maintains the porosity of the outer enamel lesion surface to promote the remineralization of the inner portions of the lesion. One group of enamel samples (n = 10) were immersed in a demineralization solution maintained at 37°C for 24 hours at pH 4.9 composed of a 40 mL aliquot of 2.0 mmol/L calcium, 2.0 mmol/L phosphate and 0.075 mol/L

#213681 - $15.00 USD Received 9 Jun 2014; revised 25 Jul 2014; accepted 28 Jul 2014; published 1 Aug 2014

acetate. These samples were placed into the neutral pH remineralization solution composed of 1.5 mmol/L calcium, 0.9 mmol/L phosphate, 150 mmol/L KCl, 2 ppm F^-, and 20 mmol/L HEPES buffer maintained at pH 7.0 and 37°C [7].

It has been also shown that the supersaturated acidic calcifying solution can enhance the rate and extent of subsurface remineralization [28]. It has been hypothesized that the supersaturated acidic calcifying solution maintains the mineral ion diffusion channels within the outer enamel lesion due to the acidity of the solution. Another group of enamel samples (n = 10) were immersed in a demineralization solution maintained at 37°C for 8 hours at pH 4.6 composed of a 40 mL aliquot of 18 mmol/L calcium, 8 mmol/L phosphate, and 0.1 mol/L lactic acid. These samples were placed into acidic remineralization solution at pH 4.8 composed of a 40 mL aliquot of 4.1 mmol/L calcium, 15 mmol/L phosphate, 50 mmol/L lactic acid and 20 ppm F^- [28].

Acid-resistant varnish was applied to the windows for 0, 4, 8 and 12 day periods of remineralization. After the fourth period, the samples were removed from the remineralization solution, and the acid resistant varnish was removed by immersion in acetone in an ultrasonic bath for 15 minutes. Each sample was then stored in 0.1% thymol solution to prevent fungal and bacterial growth.

2.2 PS-OCT system

The system used in this study has been described previously [19]. An all fiber-based Optical Coherence Domain Reflectometry (OCDR) system with polarization maintaining (PM) optical fiber, high speed piezoelectric fiber-stretchers and two balanced InGaAs receivers PDR-13 that was designed and fabricated by Optiphase, Inc., Van Nuys, CA was used to acquire the images. This two-channel system was integrated with a broadband superluminescent diode (SLD) DL-CS3159A, Denselight (Jessup, MD) and a high-speed XY-scanning system (ESP 300 controller & 850G-HS stages, National Instruments, Austin, TX) for *in-vitro* optical tomography. This system is based on a polarization-sensitive Michelson interferometer [29]. The high power (15 mW) polarized SLD source operated at a center wavelength of 1317 nm with a spectral bandwidth full-width-half-maximum (FWHM) of 84 nm to provide an axial resolution of 9 μm in air and 6 μm in enamel (refractive index = 1.6). This light was aligned with the slow axis of the PM-fiber of the source arm of the interferometer. The sample arm was coupled to an anti-reflectance (AR) coated fiber-collimator to produce a 6 mm in diameter, collimated beam. That beam was focused onto the sample surface using a 20 mm focal length AR coated plano-convex lens. This configuration provided a lateral resolution of approximately 20 μm with a dynamic range of 48 dB. Both orthogonal polarization states of the light scattered from the tissue were coupled into the slow and fast axes of the pm-fiber of the sample arm. A quarter wave plate set at 22.5° to horizontal in the reference arm rotated the polarization of the light by 45° upon reflection. After being reflected from the reference mirror and the sample, the reference beams were recombined by the pm fiber-coupler. A polarizing cube splits the recombined beam into its horizontal and vertical polarization components or “slow” and “fast” axis components, which were then coupled by single mode fiber optics into two detectors. The light from the reference arm was polarized at 45° and therefore split evenly between the two detectors. Readings of the electronically demodulated signal from each receiver channel represent the intensity for each orthogonal polarization of the backscattered light. Neutral density filters are added to the reference arm to reduce the intensity noise for shot limited detection. The all-fiber OCDR system is described in reference [29].

The PS-OCT system was completely controlled using LabView™ software (National Instruments, Austin, TX). Each B-scan consisted of 300 A-scans spaced 50 μm apart. The A-scan sweep rate was 100 Hz and each A-scan was averaged 10 times. The total number of data points in each A-scan was 2000 over a scan range of approximately 7 mm in air.

#213681 - $15.00 USD Received 9 Jun 2014; revised 25 Jul 2014; accepted 28 Jul 2014; published 1 Aug 2014

2.3 Image processing

Images obtained from the PS-OCT were processed using a dedicated program constructed with Labview™ software. The automated image processing method is based on a previous study [30]. There is a phase shift in PM-fiber between the two axes and the axial position calibration was performed only once prior to the study. A gold mirror was scanned at 100 Hz scan sweep rate and each A-scan was averaged 100 times. One hundred A-scans were acquired at 50 μm intervals over the entire scan range to determine the required axial position adjustments and the axial position of the cross-polarization scan images was adjusted to match the co-polarization scan images.

Background subtraction was carried out by subtracting the mean reflectivity of 200 data points measured in air acquired from the top 4 pixels of the 50 unprocessed A-scans outside the sample area for each B-scan. Those 200 data points provided consistent information about the system noise and manifested a standard deviation smaller than 0.01 dB. Tomographic images of the sample were reconstructed from B-scans. The images were convolved with a 5x5x5 anisotropic diffusion Gaussian smoothing filter with σ (= 4 μm) based on the μm/pixel ratio of sound enamel in each axis in order to reduce speckle noise. A 5x5 rotating kernel transformation (RKT) technique was applied in x-z and y-z spaces to emphasize thin edges while further suppressing speckle noise [31]. We determined that the 5x5x5 anisotropic diffusion Gaussian smoothing filter and the 5x5 RKT filter yielded the highest contrast of the transparent surface layer.

2.4 Transparent surface layer detection and measurement

Edge detection was applied to each A-scan using the zero-crossing first-order derivative. The position of the maximum peak of each A-scan was designated as the first peak and the respective edges of the first peak were found by locating the pixels for which the magnitude of the gradient exceeded a certain minimum for at least 4 consecutive pixels. If those edges were found, a second peak was located by searching for the maximum peak intensity outside of the initial edges. The intensity values of the two peaks were required to be greater than 3 standard deviations of the noise. The ratio of intensity values of the two peaks was required to be above a threshold of 0.1 and the ratio of the intensity values of the edge and the second peak was required to be less than a threshold of 0.75. If two peaks were found, the algorithm assumed the upper positioned peak to be the surface reflection and the lower positioned peak to be in lesion body. By carefully adjusting the threshold values, it was possible to detect only the desired peaks and ignore peaks that were too small, too wide, or too narrow, thus reducing false-positives [26]. These threshold values were specific to this PS-OCT system and the same threshold values were applied to all the samples.

The position of the strong surface reflection in the co-polarization axis and the strong scattering of polarized light from the underlying lesion body in the cross-polarization axis are used as previously described in the three diagrams of Fig. 2 in ref [26]. In this study, binary images were generated to indicate either the presence or absence of the transparent surface layer and a 5x5 morphological closing operation with a 50% threshold was subsequently applied to the binary images in order to reduce false-negatives. Pixels were converted to microns in enamel using a refractive index correction of 1.6 to yield the final transparent surface layer thickness. The thickness of the transparent surface layer was estimated by averaging 25 A-scans from a 5x5 region of interest. A 5x5 median filter was applied to the final 2D projection image of the transparent surface layer thickness for improved visualization.

2.5 Lesion depth measurement

The previously developed algorithm to calculate the lesion depth utilized a threshold of $1/e^2$ of the peak maximum [30]. We compared that approach with an algorithm that utilizes the

#213681 - $15.00 USD Received 9 Jun 2014; revised 25 Jul 2014; accepted 28 Jul 2014; published 1 Aug 2014

full-width-half-maximum (FWHM). Images acquired in a previously study (n = 34) were analyzed [32] using the two methods. An edge locator was used to make two passes along each A-scan of the processed CP-OCT images to locate the respective positions at which the intensity has decreased to the threshold calculated with either $1/e^2$ or half of the lesion peak maximum. A linear relationship was established between the lesion depth using PS-OCT and the histological lesion depths measured using polarized light microscopy (PLM) [32]. Based on this relationship, the goodness of fit, R^2, was compared and a linear correction was applied to the lesion depth calculated from CP-OCT.

2.6 Integrated reflectivity measurement (ΔR)

Previous studies have shown that the integrated reflectivity, ΔR, over the estimated lesion depth positively correlates with the integrated mineral loss (volume percent mineral loss × μm), ΔZ [20, 21]. A region of interest (ROI) was specified for the sound region from each sample in order to discriminate between demineralized and sound enamel. ΔR was calculated from the selected ROI and it was compared to the ΔR of the lesions in order to reduce false-positives in lesion detection. Remineralized lesions do not typically yield a complete reversal of demineralization and the original lesion body is partially retained under the transparent surface layer [5]. ΔR was calculated by integrating from the base of the transparent layer through the entire estimated lesion body in the CP-OCT images. This had the added advantage of removing the contribution of the high specular reflection at the surface of the transparent layer, which was large enough to be present even in the CP-OCT images. A 5x5 median filter was applied to the final 2D projection image of ΔR for improved visualization.

2.7 Polarized light microscopy (PLM) and transverse microradiography (TMR)

After sample imaging was completed, approximately 200 μm thick serial sections were cut using an Isomet 5000 saw (Buehler, IL), for polarized light microscopy (PLM) and transverse microradiography (TMR). PLM was carried out using a Meiji Techno Model RZT microscope (Meiji Techno Co., LTD, Saitama, Japan) with an integrated digital camera, Canon EOS Digital Rebel XT (Canon Inc., Tokyo, Japan). The sample sections were imbibed in water and examined in the brightfield mode with crossed polarizers and a red I plate with 500 nm retardation. PLM images were acquired at 350x magnification and had a resolution of 3264 x 2448 pixels.

A custom built digital microradiography (TMR) system was used to measure the volume percent mineral content in the areas of demineralization on the tooth sections [33]. High-resolution microradiographs were taken using Cu Kα radiation from a Philips 3100 X-ray generator and a Photonics Science FDI X-ray digital imager, Microphotonics, (Allentown, PA). The X-ray digital imager consists of a 1392 × 1040 pixel interline CCD directly bonded to a coherent micro fiber-optic coupler that transfers the light from an optimized gadolinium oxysulfide scintillator to the CCD sensor. The pixel resolution is 2.1 μm, and the images can be acquired in real time at a frame rate of 10 fps. A high-speed motion control system with Newport (Irvine, CA) UTM150 and 850G stages and an ESP 300 controller coupled to a video microscopy and laser targeting system was used for precise positioning of the tooth sample in the field of view of the imaging system. Sections with uneven thickness or fractured surface were excluded from statistical analysis.

2.8 Statistical analysis

Sample groups were compared using repeated measures analysis of variance (ANOVA) with a Tukey–Kramer post hoc multiple comparison test. Linear regression with Pearson's correlation was used to examine the relationship between data acquired from PS-OCT, PLM and TMR measurements, including sound, demineralization and remineralization areas. All statistical analyses were performed with 95% confidence with Prism™ (GraphPad software, San Diego, CA).

#213681 - $15.00 USD Received 9 Jun 2014; revised 25 Jul 2014; accepted 28 Jul 2014; published 1 Aug 2014

3. Results

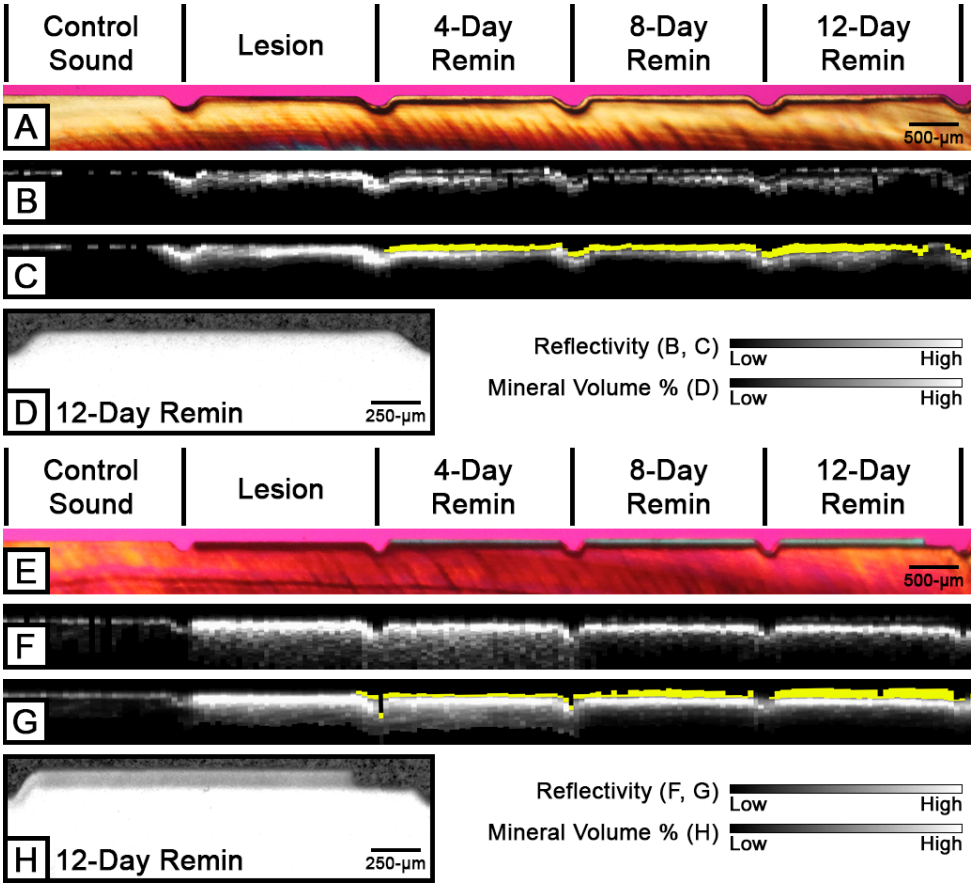

Fig. 1. PLM, CP-OCT and TMR images of the samples from the acidic pH remineralization model (A-D) and the neutral pH remineralization model (E-H) for the four time periods of exposure to the remineralizing solution. PLM (A and E) and CP-OCT B-scans (unprocessed B and F; processed C and G) show decreased depth of the lesion body as well as an increase in transparent surface layer thickness over the periods of exposure to remineralizing solution. The transparent surface layer is highlighted in yellow in PS-OCT images. TMR (D and H) shows increased mineralization of the lesion after exposure to remineralizing solution for 12 days.

Figure 1 shows PLM images, CP-OCT B-scans and TMR images of the samples prepared with the acidic pH remineralization model (A-D) and the neutral pH remineralization model (E-H). A transparent surface layer due to remineralization is clearly visible in both models with PLM, TMR and OCT. The transparent surface layer that was automatically detected with the software is highlighted in yellow in the OCT images as shown in Figs. 1(C) and 1(G). The two remineralization models produce markedly different structures. The neutral pH remineralization model produced new mineral predominantly along the surface of the enamel lesion as shown in the TMR image (Fig. 1(H)). There was minimal mineralization of the body of the lesion with this approach [34]. However, the acidic pH remineralization model produced mineralization in the lesion body as shown in Fig. 1(D). Although mineralization was incomplete in this region compared to the sound enamel structure, it was much higher than the corresponding region produced with the neutral pH remineralization model. Some samples exposed to the acidic pH remineralization model exhibited demineralization of the surface of the transparent surface layer, which goes through constant demineralization at low

#213681 - $15.00 USD Received 9 Jun 2014; revised 25 Jul 2014; accepted 28 Jul 2014; published 1 Aug 2014

pH with continued nucleation of fluorapatite [28]. These models represent different variations of demineralization and remineralization that occur in the oral cavity.

The automated transparent surface layer detection algorithm was able to successfully detect the transparent surface layers. The smallest surface layer thickness detectable was 4 pixels (10 µm). Detection of the transparent surface layer with PLM and TMR is limited due to "edge-effects" which varied from 0 µm to 35 µm for the 200 µm thick sections. Edge-effects are caused by the uneven sample surface, which is often not perfectly perpendicular to the serial cut sections. The edge-effects in PLM can be seen as a blurry shadow at the edge of the sample and at the interface of the two materials such as the dentino-enamel junction, and the edge-effects in TMR result in underestimation of the volume percent mineral leading to inaccurate integrated mineral loss. It was possible to detect transparent surface layers smaller than 10 µm with PLM for some samples with minimal edge-effects [22]. OCT does not suffer from edge-effects since it does not require serial cut sections. The algorithm detected the lesions with transparent surface layers with high sensitivity (0.92) and high specificity (0.97) compared with PLM, and the algorithm detected all the lesions with transparent surface layers thicker than 10 µm. The total number of windows was 80 from 20 samples with 44 true positives, 1 false-positive, 31 true-negatives and 4 false-positives. The thickness of the transparent surface layer estimated with PS-OCT showed a strong correlation with PLM measurements (Pearson's correlation, $p < 0.0001$, $R^2 = 0.90$) as shown in Fig. 2.

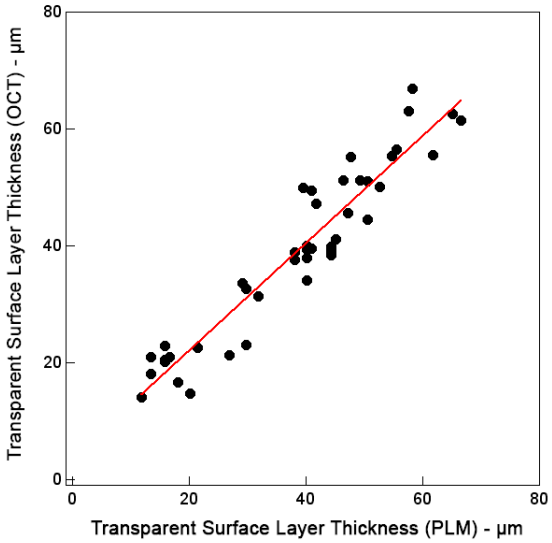

Fig. 2. A plot of transparent surface layer thickness estimated from the automated algorithm (PS-OCT) vs. thickness determined with histology (PLM). Only the true-positive windows are shown above (n = 44).

The intensity of the lesion body is reduced due to attenuation and dispersion from the transparent surface layer and use of a threshold of $1/e^2$ of the peak maximum of the lesion body in the cross-polarization axis scan overestimates the lesion body depth. Although the accurate estimation of the depth of the lesion body is confounded by dispersion from the thick transparent surface layer, approximation of the depth of the lesion body is still necessary in order to calculate the integrated reflectivity. Thus, the previously proposed algorithm for estimating lesion depth employing $1/e^2$ width of the peak maximum was compared to the one employing FWHM. The half value of the peak maximum provided a threshold that was well above 3 standard deviations of the noise and the variable intensity caused by birefringence banding in the enamel for most samples [13]. Enamel is composed of highly oriented hydroxyapatite crystals and changes in crystal orientation cause changes in birefringence,

#213681 - $15.00 USD Received 9 Jun 2014; revised 25 Jul 2014; accepted 28 Jul 2014; published 1 Aug 2014

which show up as banding artifacts in PS-OCT images. Comparison with the PLM measurements indicated that the method that employed FWHM (Pearson's correlation, $p < 0.0001$, $R^2 = 0.91$) yielded higher correlation compared to the method that employed the $1/e^2$ width of the peak maximum (Pearson's correlation, $p < 0.0001$, $R^2 = 0.76$). Based on this relationship, linear regression was employed to correct the OCT lesion depth (Corrected lesion depth = 2.694 × OCT pixel depth – 27.5). The corrected lesion depth and the depth of the lesion body underlying the transparent surface layer were estimated with PS-OCT by using FWHM as a threshold. Figure 3 shows strong correlation (Pearson's correlation, $p < 0.0001$, $R^2 = 0.58$) of the corrected lesion depth measured with PS-OCT and the lesion depth measured with PLM for the windows that did not exhibit the transparent surface layer (true-negatives). However, when the estimated depth measurements of the lesion body of all windows that exhibited the transparent surface layer (true-positives) with PS-OCT were compared with the depth measurements with PLM, there was a significant reduction in the correlation (Pearson's correlation, $p = 0.0258$, $R^2 = 0.11$) as well as an overestimation of the depth of the lesion body due to dispersion from the varying thickness of the transparent surface layer.

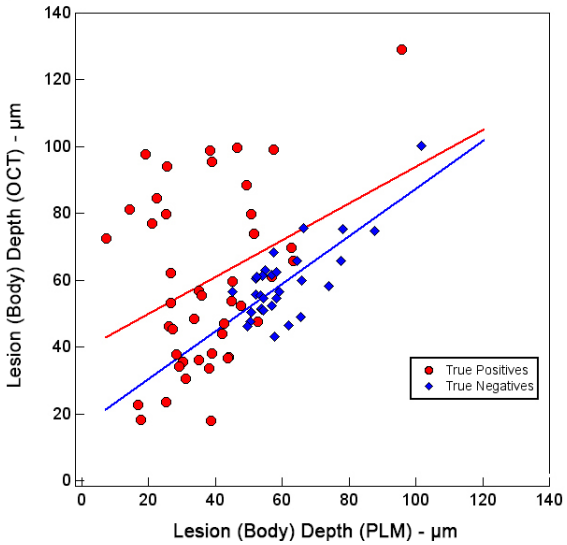

Fig. 3. A plot of estimated lesion (body) depth measurements vs. lesion (body) depth determined with histology (PLM). True-positive windows exhibited the transparent surface layer with both PS-OCT and PLM (n = 44). True-negative windows did not exhibit the transparent surface layer with both PS-OCT and PLM (n = 31). The FWHM method was used for lesion (body) depth estimation. The line with matching color represents the best-fit line.

#213681 - $15.00 USD Received 9 Jun 2014; revised 25 Jul 2014; accepted 28 Jul 2014; published 1 Aug 2014

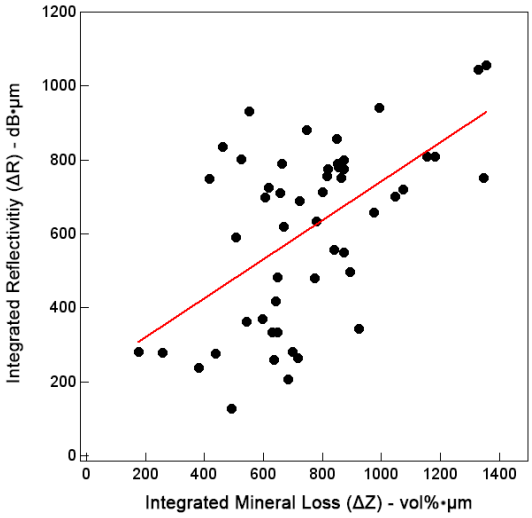

Fig. 4. A plot of integrated reflectivity, ΔR, over the estimated lesion (body) depth (PS-OCT) vs. integrated mineral loss, ΔZ, over 200 μm (TMR). Windows with uneven thickness or fractured surface were excluded from the comparison (n = 52).

The integrated reflectivity, ΔR, over the estimated depth of the lesion body and the integrated mineral loss, ΔZ, of the windows with uniform thickness (n = 52) exhibited a moderate correlation (Pearson's correlation, $p < 0.0001$, $R^2 = 0.32$) as shown in Fig. 4. TMR is also prone to edge-effects due to the 200 μm section thickness and most of the lesions are shallow, less than 100 μm. In addition, the mineral loss in the area was small ~5%, which is difficult to resolve with TMR. The lesion severity and the thickness of transparent surface layer measurements for PS-OCT, PLM and TMR are tabulated in Table 1 for both models.

Table 1. Mean ± S.D. of PS-OCT, PLM and TMR measurements for the four periods of exposure to the remineralizing solution. Groups with the same letter are statistically similar, P > 0.05 in each row.

	0-Day	4-Day	8-Day	12-Day
Acidic pH Remineralization Model (n = 10)				
Transparent Layer Thickness (PS-OCT, μm)	9.2 ± 13.7 a	42.8 ± 12.2 b	44.4 ± 9.7 b	48.8 ± 10.5 b
Transparent Layer Thickness (PLM, μm)	10.6 ± 15.9 a	40.5 ± 11.5 b, c	45.1 ± 10.2 b, d	50.5 ± 8.7 c, d
Integrated Reflectivity, ΔR (dB•μm)	483 ± 172 a	402 ± 118 a, b	346 ± 148 b, c	299 ± 119 c
Integrated Mineral Loss**, ΔZ (vol%•μm)	800 ± 141 a	683 ± 180 a, b	612 ± 235 a, b	469 ± 201 b
Neutral pH Remineralization Model (n = 10)*				
Transparent Layer Thickness (PS-OCT, μm)	0 a	8.2 ± 10.6 a	9.0 ± 16.1 a	11.3 ± 18.0 a
Transparent Layer Thickness (PLM, μm)	0 a	5.8 ± 9.2 a	8.5 ± 13.3 a	10.3 ± 15.3 a
Integrated Reflectivity, ΔR (dB•μm)	805 ± 142 a	826 ± 137 a, b	767 ± 126 b	694 ± 134 c
Integrated Mineral Loss***, ΔZ (vol%•μm)	1017 ± 250 a	911 ± 265 a, b	772 ± 168 b	615 ± 132 b

* In half of the samples, the transparent surface layer was not visible using PLM.
**n = 5 and ***n = 8, samples with uneven thickness or fractured surface were excluded from TMR analysis.

#213681 - $15.00 USD Received 9 Jun 2014; revised 25 Jul 2014; accepted 28 Jul 2014; published 1 Aug 2014

The transparent surface layer thickness and ΔR, lesion severity, can be displayed as 2D projection images in order to aid in visualization of the lesion. Surface projection images of a sample prepared via the acidic pH remineralization model are shown in Fig. 5. Selection of the sound region as a control allowed better discrimination of the sound and demineralized enamel.

4. Discussion

It is challenging to simulate the complex processes of demineralization and remineralization that occur in the oral cavity with a single *in-vitro* model [35]. The use of two different demineralization and remineralization models in this study produced transparent surface layers that varied markedly. It is believed that the remineralization process *in-vivo* is not simple superficial mineral deposition that leads to lesion arrestment. It is suspected that it is mostly due to a repair of the existing enamel crystal remnants [27]. In addition, there is likely a constant intra-oral mechanical force that prevents cariogenic plaque accumulation and superficial mineral deposition [36]. It is highly unlikely that the superficial mineral deposition that was shown with the neutral pH remineralization model (Figs. 1(E)-1(H)) replicates the remineralization process *in-vivo*. The acidic pH remineralization model showed increased mineral deposition in the lesion body (Figs. 1(A)-1(D)), which appears to better emulate *in-vivo* remineralization. It is encouraging that the algorithm was able to detect both transparent surface layer types with varying mineral profiles.

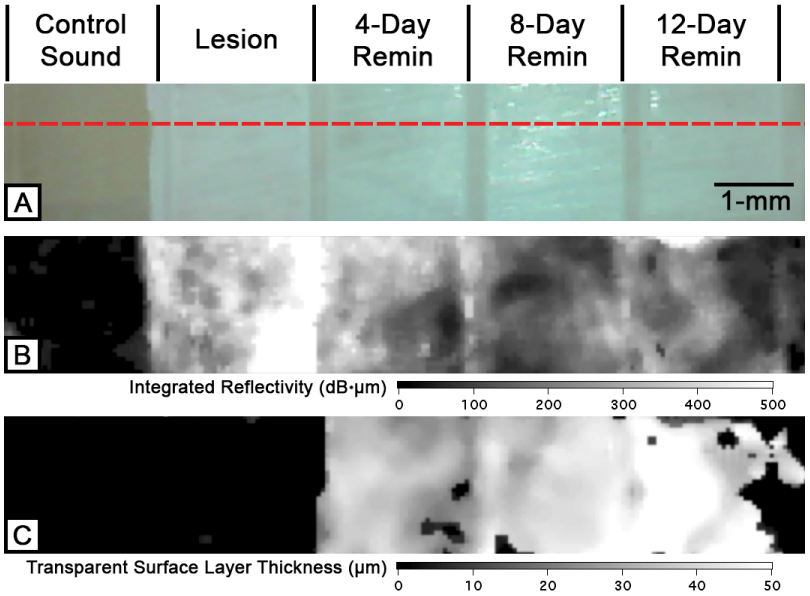

Fig. 5. Two-dimensional projection images of the acidic pH remineralization sample. A red dotted line in the visible light reflectance image (A) represents the section shown in Figs. 1(A)-1(C). Two-dimensional OCT surface projection images of the same sample are shown including (B) the integrated reflectivity and (C) the transparent surface layer thickness.

Although it was computationally intensive, the incorporation of 3D image-processing approaches such as the RKT and the anisotropic diffusion Gaussian convolution filter dramatically improved image quality compared to processing 2D B-scans individually as used in our previous OCT studies. The anisotropic diffusion Gaussian convolution filter accurately accounted for the difference between axial and transverse resolution in 3D versus 2D and the RKT filter was able to highlight the continuity of edges in 3D rather than in 2D. This enabled more accurate measurement of the transparent surface layer. In addition, using FWHM as opposed to $1/e^2$ width for the peak maximum resulted in higher correlation with histology as

#213681 - $15.00 USD Received 9 Jun 2014; revised 25 Jul 2014; accepted 28 Jul 2014; published 1 Aug 2014

well as better differentiation from artifacts caused by the optical system and the enamel birefringence. Dispersion from the transparent surface layer may have caused the depth of the lesion body to be over-estimated as shown in Fig. 3. The total amount of dispersion increases linearly with the length of a dispersive medium [37]. The dispersion mismatch causes broadening of the coherence function in the sample arm by unbalanced dispersion and reduction in peak intensity. Thus, the lesion body depth may be dependent on the thickness of the transparent surface layer. ΔR is not expected to change significantly due to peak broadening since the overall reflectivity should be similar. Dispersion compensation for such a highly variable composite mineral layer via correlation or deconvolution techniques is extremely complex and is beyond the scope of this study [37]. Nonetheless, the lesion severity, which is of greater interest, can still be accurately determined by calculating ΔR over the FWHM provided by the system.

This study demonstrates that PS-OCT can be used to nondestructively measure the changes in the artificial enamel lesion structure and severity upon exposure to remineralization solutions using these two different models. The automated detection and measurement of the transparent surface layer process with high sensitivity and specificity can provide extremely useful information about lesion activity to aid clinicians in the diagnosis of caries lesions. There is no accepted gold standard that can be used to differentiate between an active and an arrested lesion. The conventional lesion activity assessment methods currently available such as visual and tactile methods are not reliable and reproducible [1]. The remineralized fluorapatite rich surface layer above the lesion body has enhanced resistance to acid dissolution [5, 7, 8] and the detection of this layer with PS-OCT is of great clinical significance.

Acknowledgments

The authors acknowledge the support of NIH Grants F30-DE023278 and RO1-DE17869 and the help of Henry Tom.

#213681 - $15.00 USD Received 9 Jun 2014; revised 25 Jul 2014; accepted 28 Jul 2014; published 1 Aug 2014